Supplementary information

Materials and characterizations.

All chemicals were analytical grade and were used as received. Solutions were prepared using high purity water (Millipore Milli-Q purification system, resistivity > 18 MΩ·cm). The fluorine-doped tin oxide (FTO) conductive glass was purchased from Nippon Sheet Glass Company (Japan) and was ultrasonic cleaned with acetone, ethanol and deionized water for 20 min each in sequence prior to use. The ITO glass with a sheet resistance of 10 Ω/sq (AimCore Technology Co.Ltd) was cleaned by sequential ultrasonic treatment in detergent, deionized water, acetone, isopropanol and ethanol, ultraviolet-ozone chamber treatment for 20 min.

The obtained samples were characterized by X-ray powder diffraction (XRD) on a Rigaku D/Max-2500/PC powder diffractometer using Cu Kα radiation (operating voltage: 40 kV, operating current: 200 mA, scan rate: 5° min^{-1}). Raman spectra were measured on a Renishaw raman spectrometer with a 532 nm laser line as an exciting source. The morphologies of the electrodes were performed by a Quanta 200 FEG scanning electron microscope (SEM) equipped with an energy dispersive spectrometer (accelerating voltage of 20 kV). High resolution transmission electron microscopy (HRTEM) images were obtained on a Tecnai G2 F30 S-Twin (FEI Company) with an acceleration voltage of 300 kV. X-ray photoelectron spectroscopy (XPS) measurements were performed by Thermo ESCALAB 250Xi with monochromatized Al Kα excitation.

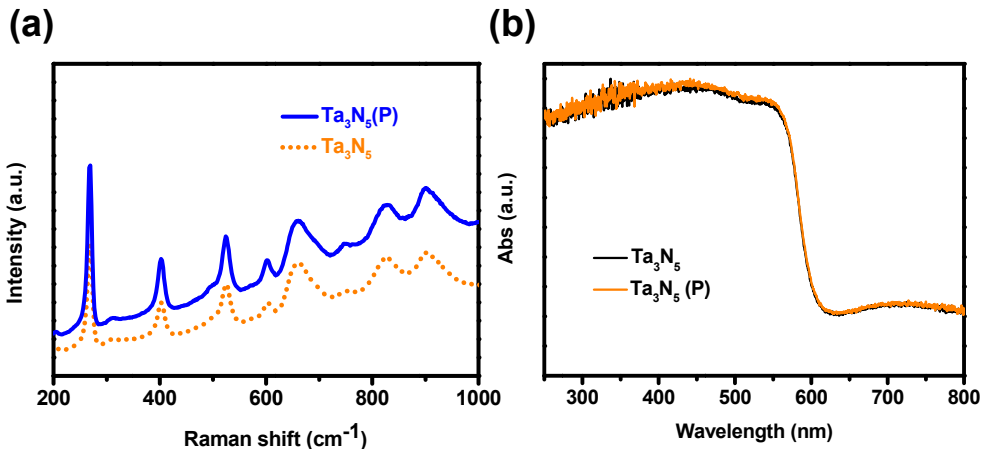

Figure S1 (a) Raman spectra of Ta_3N_5 and Ta_3N_5 (P) electrodes, which are identical with each other; exciting source: 532 nm laser. (b) UV-Vis spectra for Ta_3N_5 and Ta_3N_5 (P) powders, which shows the same bandgap of 2.06 eV; to rule out the effect of Ta substrate, we produced Ta_3N_5 and Ta_3N_5 (P) powders with the same procedure for the measurement.

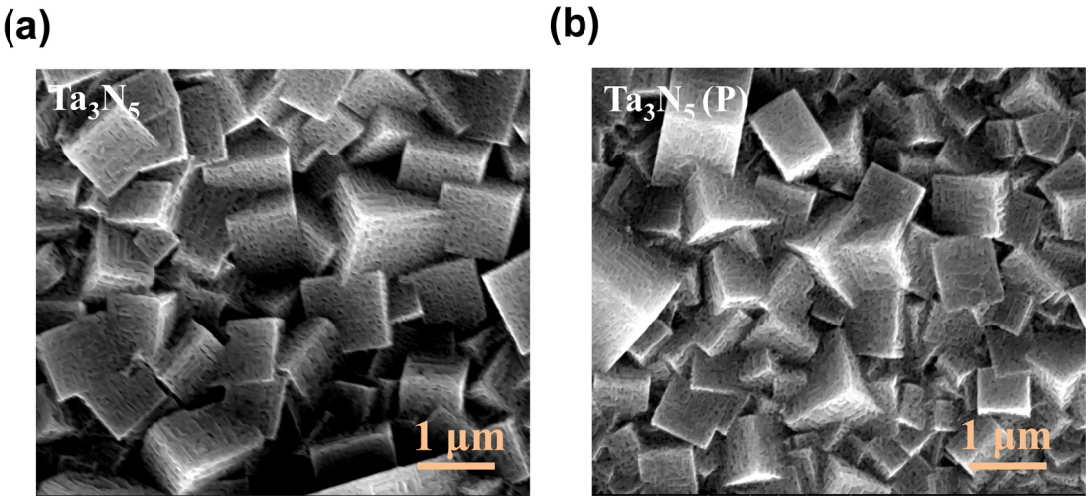

Figure S2 SEM images of (a) Ta_3N_5 and (b) Ta_3N_5 (P) electrodes.

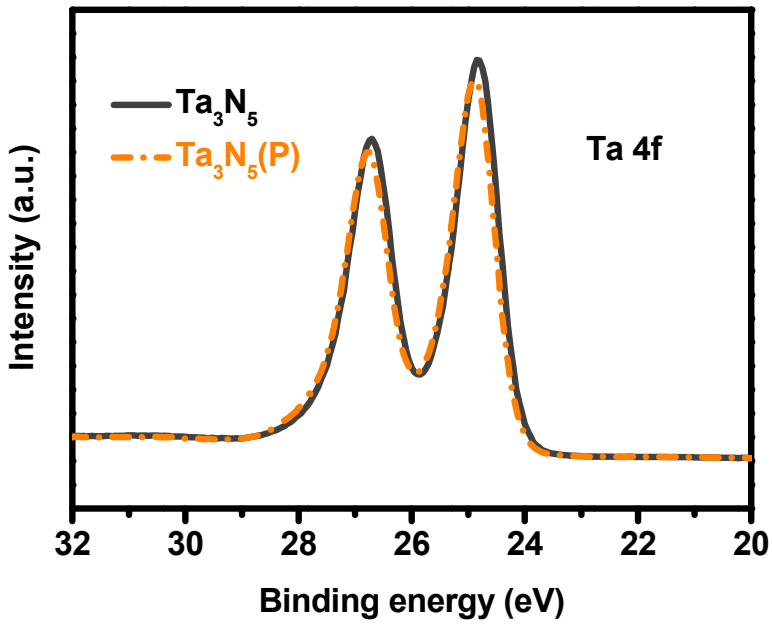

Figure S3 XPS spectra of Ta 4f for Ta_3N_5 and Ta_3N_5 (P) electrodes; The Ta 4f peak for the Ta_3N_5 (P) shifts by 0.1–0.2 eV toward higher binding energy compared with Ta_3N_5, suggesting that lower defects densities exist in the surface of Ta_3N_5 (P).[1]

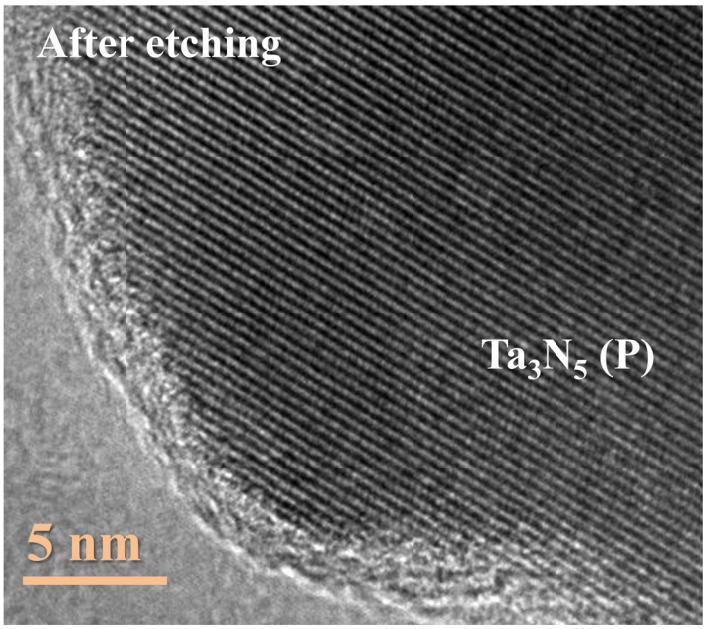

Figure S4 HRTEM image of surface etched Ta_3N_5 (P).

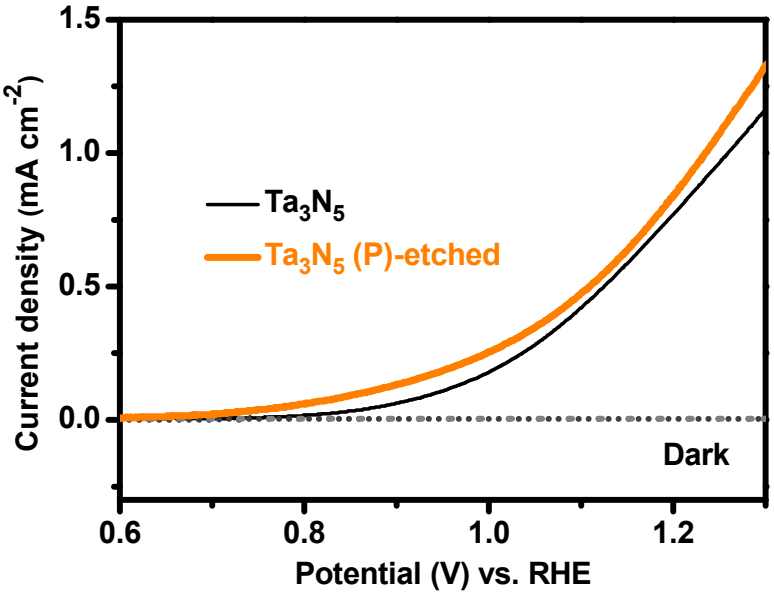

Figure S5 Current-potential curves of Ta_3N_5 and surface etched Ta_3N_5 (P) photoanodes under AM 1.5G simulated sunlight at 100 mW cm^{-2}, at 30 mV s^{-1}, in 1 M NaOH aqueous solution (pH = 13.6).

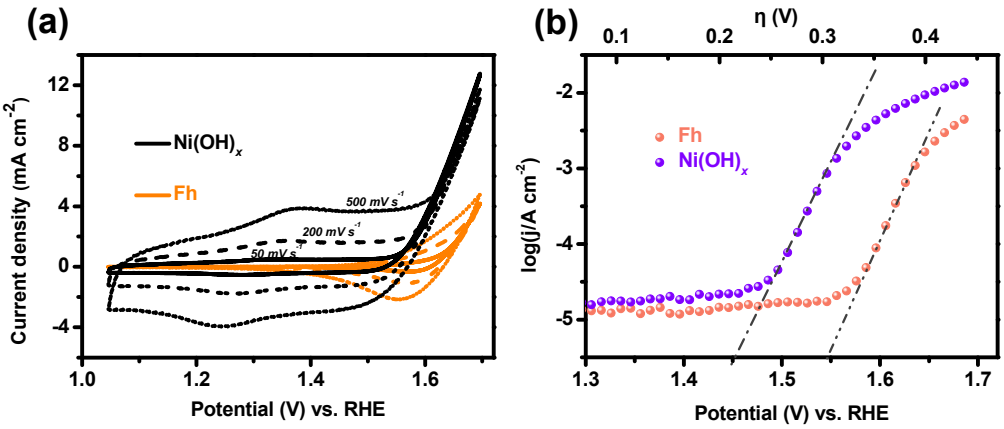

Figure S6 (a) Cyclic voltammogram (CV) diagrams for $Ni(OH)_x$/FTO and Fh/FTO with three cycles under various scan rates in 1M NaOH aqueous solution (pH = 13.6). (b) Tafel plots of $Ni(OH)_x$/FTO and Fh/FTO.

It is evident that the pseudocapacitive charging of $Ni(OH)_x$ occurs at much lower potential regions than that of Fh. Based on the fact that the kinetic overpotential of

$Ni(OH)_x$ for water oxidation is also lower than that of Fh, it is anticipated that the serial application of Fh and $Ni(OH)_x$ leads to potential gradient for consecutive hole harvesting from Ta_3N_5.

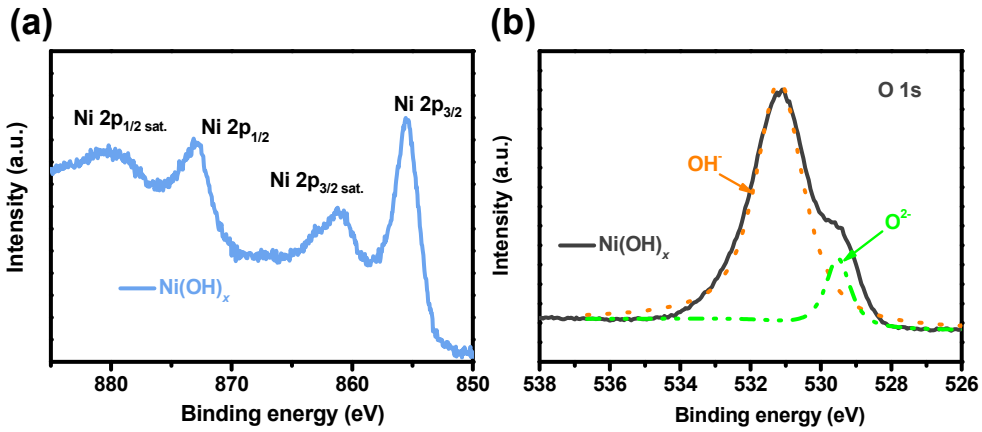

Figure S7 XPS spectra of (a) Ni 2p and (b) O 1s for the $Ni(OH)_x$/FTO. The Ni 2p binding energies at 855.6 and 873.2 eV are for Ni $2p_{3/2}$ and Ni $2p_{1/2}$, respectively, implying a mixture of Ni^{2+} and Ni^{3+}.[2, 3] The O 1s spectrum is fitted with two peaks at~529.5 and ~531.0, which are corresponded to oxide and hydroxyl species respectively. The hydroxyl species are apparently dominant in the surface of $Ni(OH)_x$.

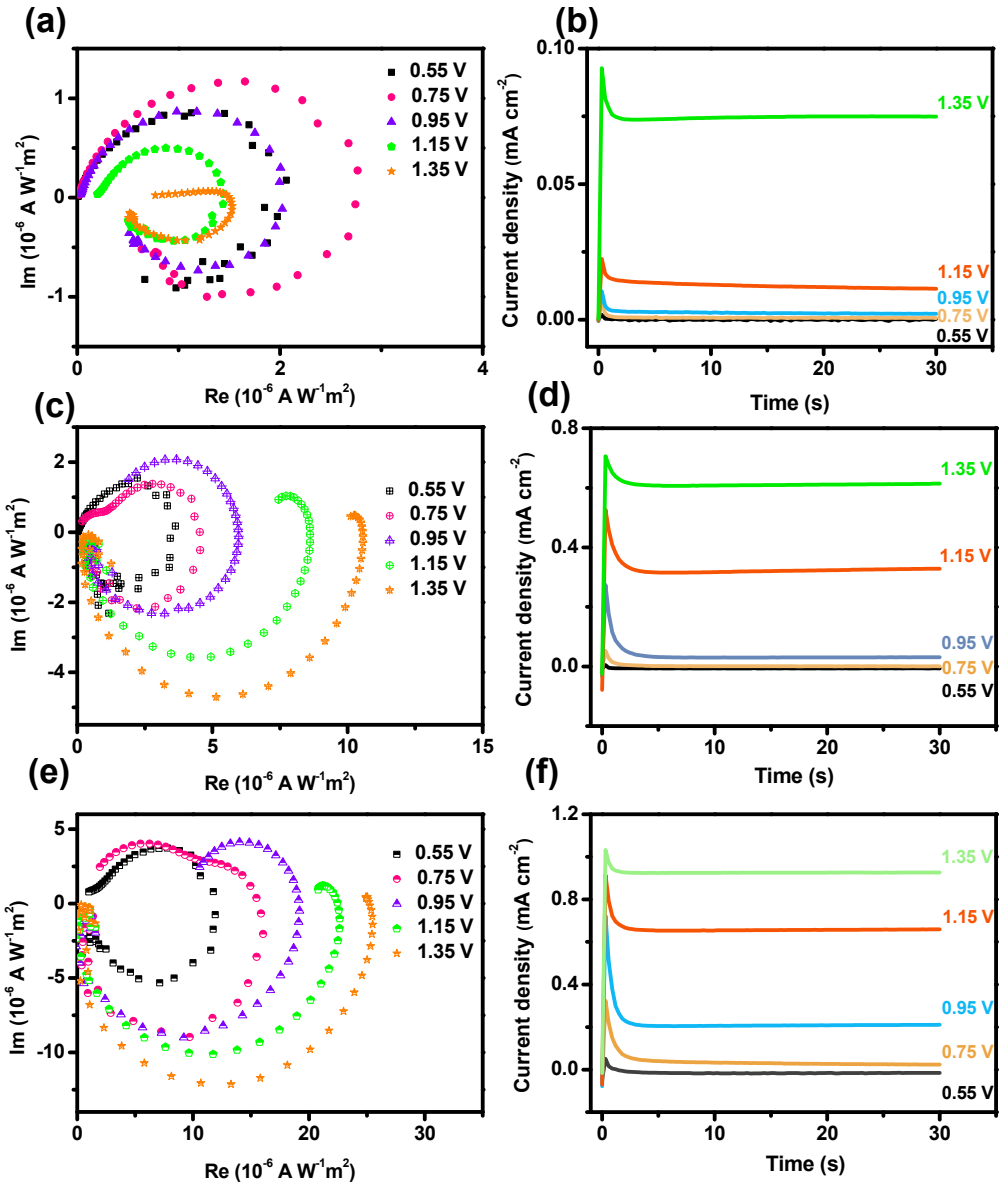

Figure S8 (a), (c) and (e): IMPS responses of Ta_3N_5 (P), Fh/Ta_3N_5 (P) and Ni(OH)$_x$/Fh/Ta_3N_5 (P) photoanodes in 1 M NaOH aqueous solution (pH = 13.6) with different applied potentials. (b), (d) and (f): The corresponding chronoamperometry measurements of the Ta_3N_5 (P), Fh/Ta_3N_5 (P) and Ni(OH)$_x$/Fh/Ta_3N_5 (P) photoanodes under 533 nm irradiation.

When the electrode is illuminated, an almost instantaneous hole current flows into the surface. Due to the electron-hole recombination, the photocurrent measured in the external circuit falls from its initial value as the electron current increases towards its

steady state value,[4] as shown in Fig. S 8(b), (d) and (f). Consequently, the time constant ($k_r + k_t$) associated with this recombination process is given by the radial frequency of the maximum of the IMPS response in the low frequency range; and the ratio: $k_t/(k_r + k_t)$ can be acquired from the ratio of the steady state photocurrent to the instantaneous photocurrent observed when the illumination is switched on.[5] The high frequency IMPS response, on the other hand, corresponds to the charge transport into the surface since the effects of surface recombination are effectively 'frozen out'. Accordingly, the average lifetime of photogenerated electrons (τ_d) can be estimated from the frequency at the minimal value in the IMPS.[6]

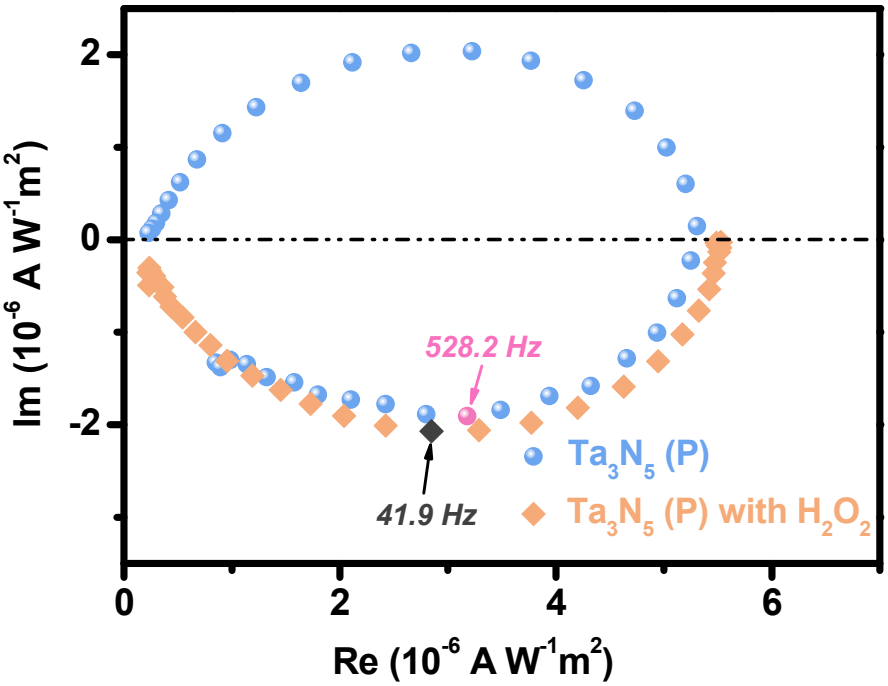

Figure S9 The comparison of IMPS responses for Ta_3N_5 (P) photoanode in 1 M NaOH and 1 M NaOH-0.5 M H_2O_2 aqueous solution (pH = 13.6) at 1.05 V.

The frequency at the minimal value in the IMPS (f_{min}) of Ta_3N_5 (P) has changed from

528.2 to 41.9 Hz by the addition of H_2O_2, indicating that the electron lifetime has been increased by 10 times with the hole scavenger. Moreover, the semicircle in the upper quadrant no longer exists since the surface recombination for H_2O_2 oxidation is supposed to be negligible.[7]

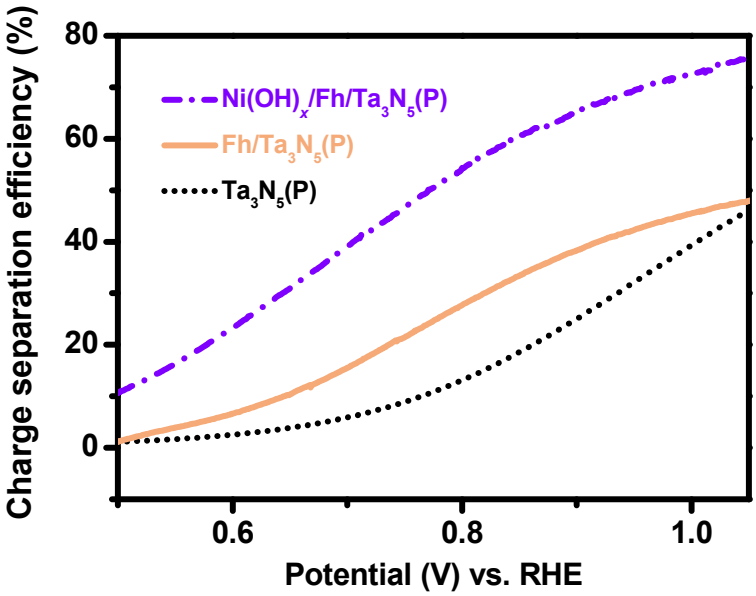

Figure S10 Charge separation efficiency versus potential curves of Ta_3N_5 (P), Fh/Ta_3N_5 (P) and $Ni(OH)_x/Fh/Ta_3N_5$ (P) photoanodes.

In principle, the photocurrent of water splitting ($J^{H_2O}_{photocurrent}$) is a product of the rate of photon absorption expressed as a current density ($J_{absorbed}$), the charge separation yield of the photogenerated carriers ($P_{charge\ separation}$), and charge injection yield to the electrolyte ($P_{charge\ injection}$):[7]

$$J^{H_2O}_{photocurrent} = J_{absorbed} * P_{chargeseparation} * P_{charge\ injection} \quad (1)$$

The photocurrent measured in the electrolyte with H_2O_2 ($J^{H_2O_2}_{photocurrent}$) is only a product of $J_{absorbed}$ and $P_{charge\ separation}$, assuming the charge injection yield becomes 100% ($P_{charge\ injection} = 1$) in the presence of a hole scavenger (H_2O_2) in the electrolyte:

$$J^{H_2O}{}_{2photocurrent} = J_{absorbed} * P_{charge\ separation} \quad (2)$$

Based on equation (1) and (2), the charge injection yield can be achieved:

$$P_{charge\ injection} = J^{H_2O}{}_{photocurrent} / J^{H_2O}{}_{2photocurrent} \quad (3)$$

The charge separation yield is given by

$$P_{charge\ separation} = J^{H_2O}{}_{2photocurrent} / J_{absorbed} \quad (4)$$

Assuming complete absorption and 100% utilization of band gap photons of Ta_3N_5, a photocurrent of 12.9 mA cm^{-2} is theoretically possible under standard AM 1.5G solar illumination ($J^{Ta_3N_5\ absorbed}$).[8] Thus, the charge separation and injection efficiency of photoelectrodes can be calculated according to equation (3) and (4).

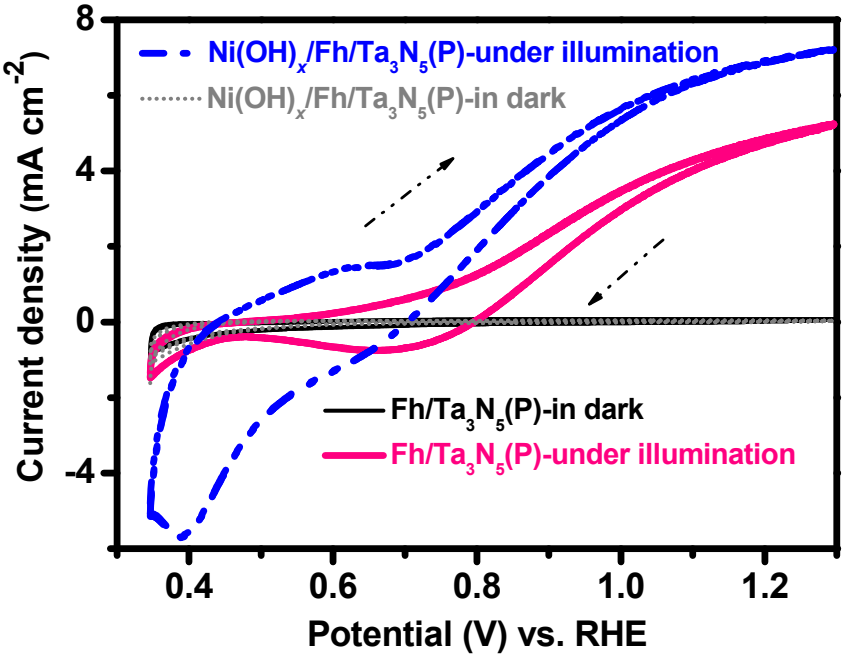

Figure S11 CV diagrams for $Ni(OH)_x/Fh/Ta_3N_5$(P) and Fh/Ta_3N_5 (P) photoanodes in 1 M NaOH aqueous solution (pH=13.6) under dark/illumination with a scan rate of 100 mV s^{-1}.

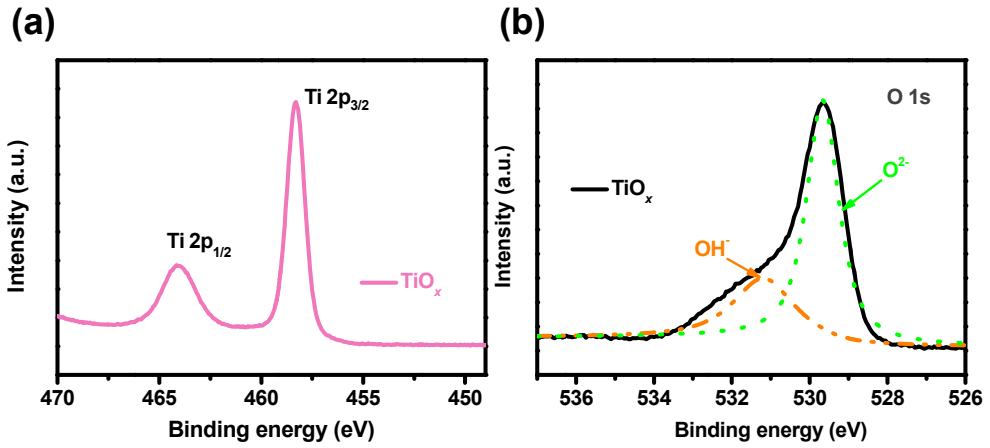

Figure S12 XPS spectra of (a) Ti 2p and (b) O 1s for the TiO_x/FTO. The Ti $2p_{3/2}$ and Ti $2p_{1/2}$ peaks are centered at a binding energy of 464.2 eV and 458.3 eV, falling between the binding energies of Ti^{4+} and Ti^{3+}.[9, 10] The O 1s spectrum is fitted with two peaks at ~529.5 and ~531.0, which are corresponded to oxide and hydroxyl species in the oxides.

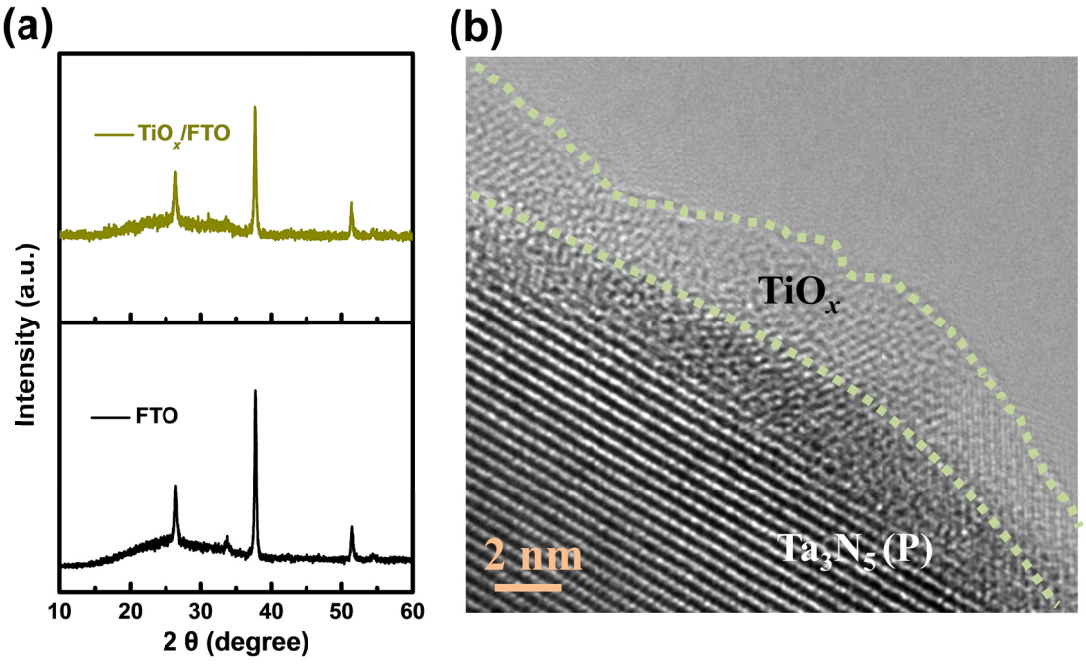

Figure S13 (a) XRD patterns of TiO_x/FTO and FTO substrate. (b) HRTEM image of TiO_x/Ta_3N_5 (P) electrode.

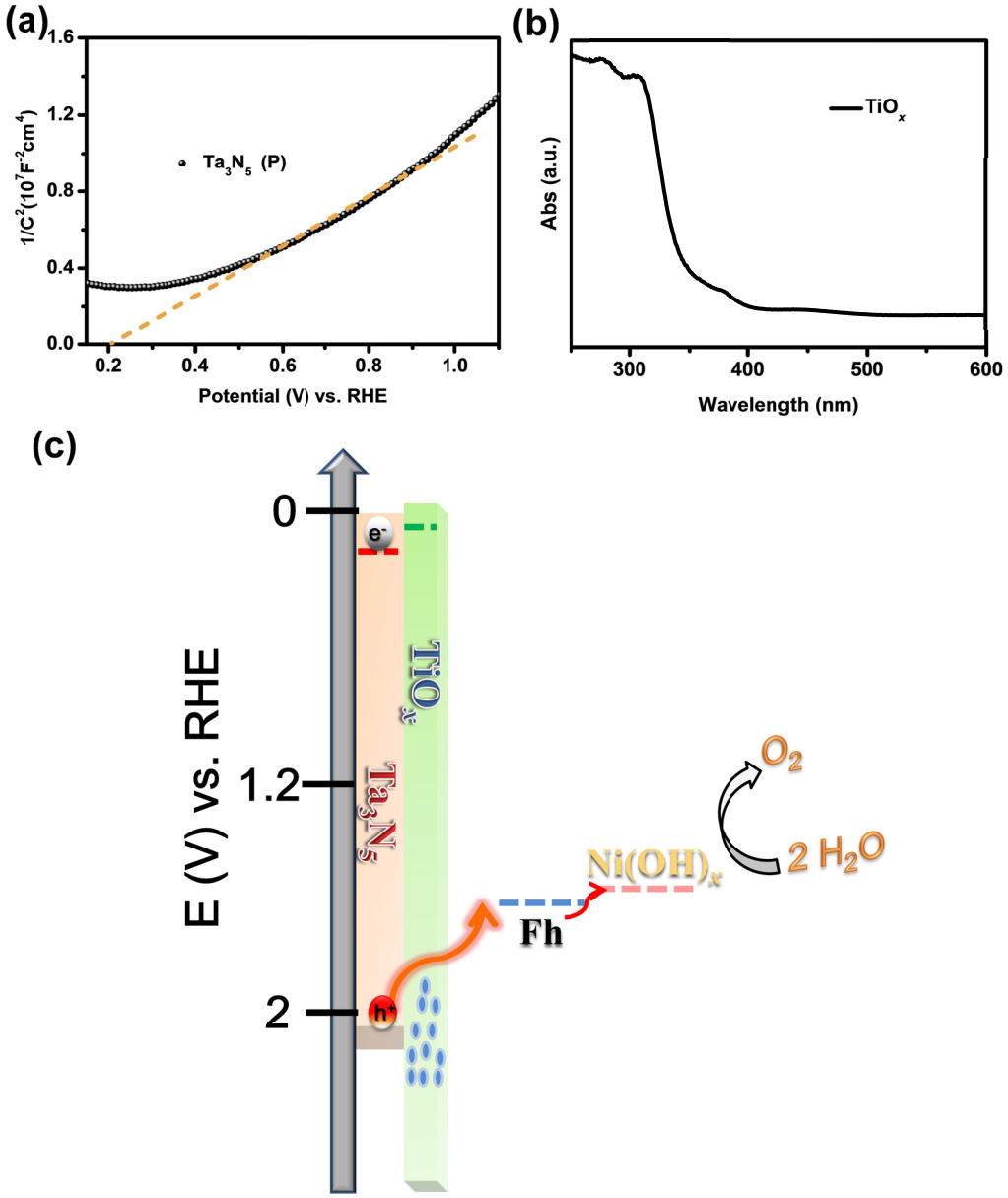

Figure S14 (a) Mott-Schottky (MS) plot of Ta_3N_5 (P) electrode in 1 M NaOH aqueous solution (pH = 13.6) with the AC potential frequency of 1000 Hz. (b) UV-Vis spectrum of TiO_x. (c) Schematic energy diagram for Ta_3N_5, TiO_x, Fh and $Ni(OH)_x$.

Fig. S14 (a) presents the Mott-Schottky (MS) measurement carried out on Ta_3N_5 (P) in 1 M NaOH electrolyte. It exhibits linear dependence with a positive slope, which is a typical feature for an n-type semiconductor and the Femi level of Ta_3N_5 (P) is close to 0.2 V, which is consistent with previous report.[11] In Fig. 5(a), the as-prepared TiO_x

exhibits a deviation from the result described by the MS equation, which is associated with the intraband electronic states.[12] As a result, the most probably energy levels of the electronic states can be obtained from the derivative of the MS plot, provided in the insert of Fig. 5(a). The potential peak at 0.05 V represents the shallow state lying near the conduction band of TiO_x. This gives rise to a 150 mV offset, comparing with the Femi level of Ta_3N_5 (P) and results in an enhancement of electron reflux barrier from Ta_3N_5 to HSL. Although the bandgap of TiO_x is found to be 3.2 eV (Fig. S14(b)), the electronic states localized at 1.25 V and 1.75 V, which are above the valence band of TiO_x, might benefit to mediate hole transport between Ta_3N_5 and HSL as presented in Fig. S14(c).

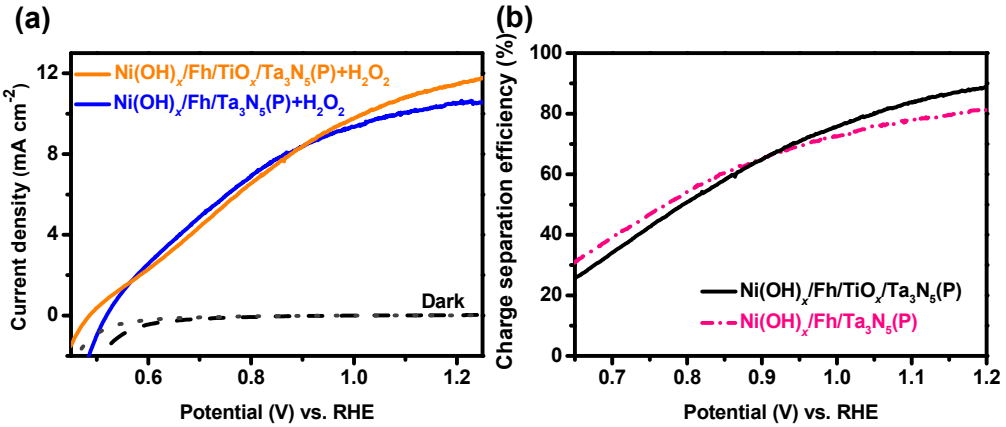

Figure S15(a) Current-potential curves of the $Ni(OH)_x/Fh/Ta_3N_5$ (P) and $Ni(OH)_x/Fh/TiO_x/Ta_3N_5$ (P) photoanodes under AM 1.5G simulated sunlight at 100 mW cm^{-2} in 1 M NaOH-0.5 M H_2O_2 aqueous solution (pH = 13.6). (b) The corresponding charge separation efficiency versus potential curves.

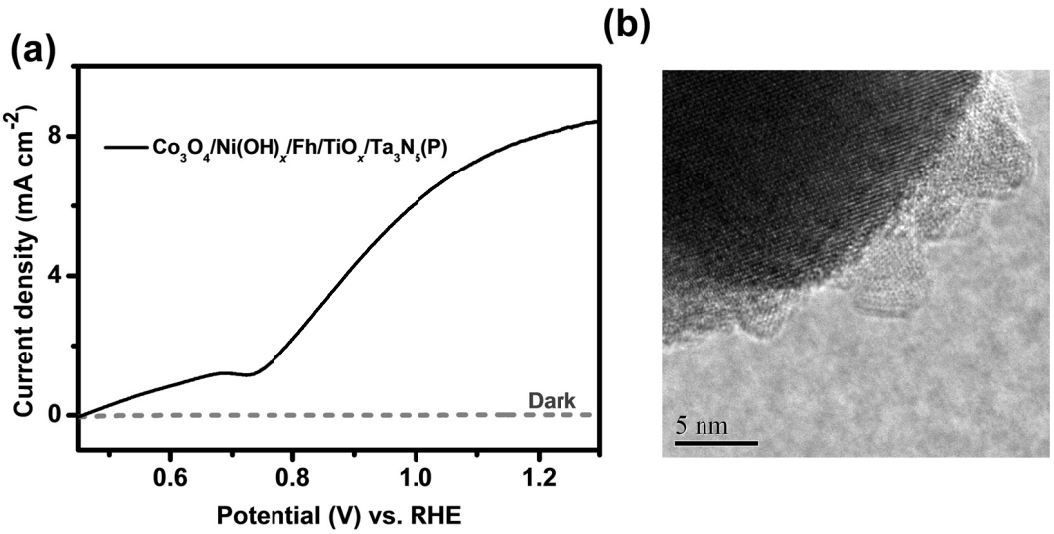

Figure S16 (a) Current-potential curve of $Co_3O_4/Ni(OH)_x/Fh/TiO_x/Ta_3N_5$ (P) photoanode under AM 1.5G simulated sunlight at 100 mW cm^{-2} in 1 M NaOH aqueous solution (pH = 13.6). (b) HRTEM of $Co_3O_4/Ni(OH)_x/Fh/TiO_x/Ta_3N_5$ (P).

Co_3O_4 nanoparticles (NPs) were introduced by hydrothermal process as we previously reported[13] and electrodes were subsequently immersed in the solution containing Co_3O_4 NPs for 3 h. Although Co_3O_4 NPs has been investigated as an efficient OEC for Ta_3N_5 photoanode,[13] the PEC performance of the $Ni(OH)_x/Fh/TiO_x/Ta_3N_5$ (P) photoanode (Fig.6(a)) is superior to that of $Co_3O_4/Ni(OH)_x/Fh/TiO_x/Ta_3N_5$ (P) (Fig. S16(a)) photoanode. It is thus reasonable to deduce that the relatively low performance with Co_3O_4 might be due to the improper contact between $Ni(OH)_x$ and Co_3O_4 NPs. As shown in Fig. S16(b), $Ni(OH)_x$ and Co_3O_4 NPs are mixed on the surface, which could result in grain boundaries.

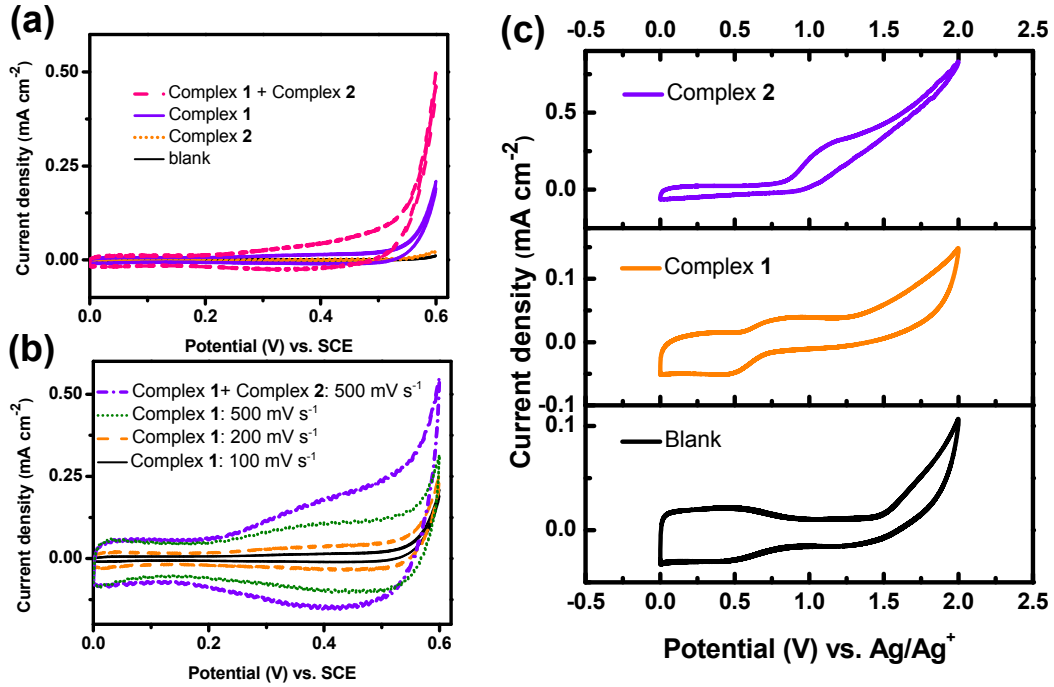

Figure S17(a) CV measurements of blank, complex **1**, complex **2** and the combination of complex **1** and complex 2 with a scan rate of 100 mV s^{-1} in 1 M NaOH. The FTO electrode, a platinum electrode and saturated calomel electrode were used as working, counter and reference electrodes, respectively. (b) CV measurements of complex **1**with scan rates of 100-500 mV s^{-1} in 1 M NaOH and the combination of complex **1** and complex 2 with a scan rate of 500 mV s^{-1}.The FTO electrode, a platinum electrode and saturated calomel electrode were used as working, counter and reference electrodes, respectively. (c) CV measurements of blank, complex **1** and complex **2** with a scan rate of 100 mV s^{-1} in anacetonitrile solution with 0.1 M tetrabutylammonium hexafluorophosphate as electrolyte. The FTO electrode, a platinum electrode and Ag/Ag^{+} electrode were used as working, counter and reference electrodes, respectively.

In Fig. S17(a), the complex **1** is much more active than complex **2** for electrochemical water oxidation (i.e., less overpotential required to achieve the same current density),

which can account for the higher photocurrent of complex **1**/$Ni(OH)_x$/Fh/TiO_x/Ta_3N_5 (P) photoanode in low bias observed in Fig. 7(b). It is also notable that the addition of complex **2** not only improves the activity of complex **1** for water oxidation but also leads to an increase of redox peaks in 0.2~0.5 V as well as a negative shift as shown in Fig. S17(b). The dramatic increase of the redox peaks with scan rate indicates that these are associated with the pseudo-capacitance of Co species as the water oxidation intermediates. These results suggest that the addition of complex **2** might participate in the catalytic cycle of complex **1** for water oxidation. To verify this, we further tested the CV of complex **1** and **2** in organic solution for probing the redox potentials of Co (III) and Ir (III) respectively, ruling out the affection of water oxidation peak (Fig S17(c)). It turns out that the potential for the oxidation of Ir (III) is close to that of the Co (III). It is possible the higher oxidation states such as Co(IV) and Co(V) could further oxidize Ir (III) for water oxidation.[14, 15] As a result, the complex **1** could bridge the hole transport pathway from HSL to complex **2** for water oxidation.

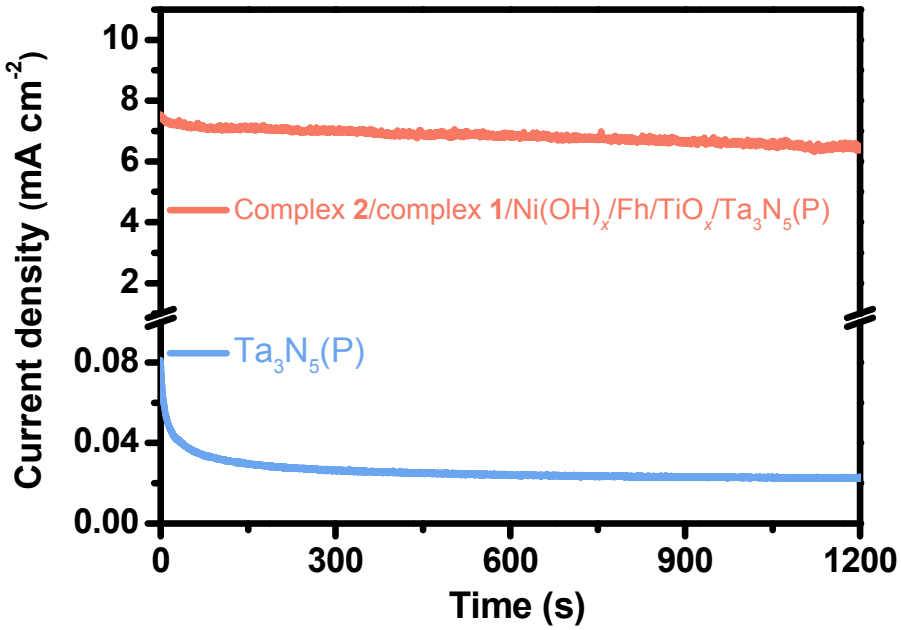

Figure S18 Chronoamperometry measurement of the Ta_3N_5 (P) and Complex **2**/complex**1**/Ni(OH)$_x$/Fh/TiO$_x$/Ta_3N_5 (P) photoanodes at 0.9 V vs. RHE under AM 1.5G simulated sunlight at 100 mW cm^{-2} in 1M NaOH aqueous solution (pH = 13.6).

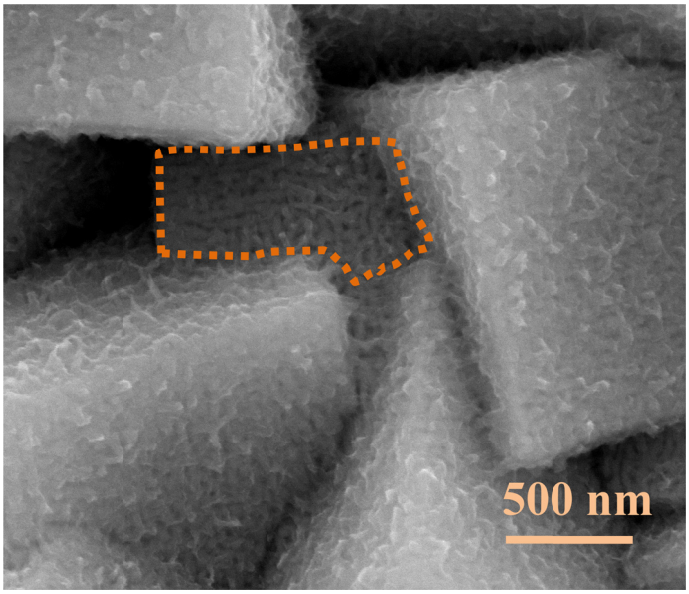

Figure S19 SEM image of the Complex **2**/complex **1**/Ni(OH)$_x$/Fh/TiO$_x$/Ta_3N_5 (P) photoanode with high resolution. The surface of Ta_3N_5 is not completely covered, especially the particles located near the substrate.

References

1. N. Arshi, J. Q. Lu, Y. K. Joo, J. H. Yoon and B. H. Koo, *Surf. Interface. Anal.,* 2015, **47**, 154-160.
2. A. P. Grosvenor, M. C. Biesinger, R. S. Smart and N. S. McIntyre, *Surf. Sci.,* 2006, **600**, 1771-1779.
3. E. L. Ratcliff, J. Meyer, K. X. Steirer, A. Garcia, J. J. Berry, D. S. Ginley, D. C. Olson, A. Kahn and N. R. Armstrong, *Chem. Mater.,* 2011, **23**, 4988-5000.
4. L. M. Peter, Chem. Rev., 1990, **90**, 753-769.
5. L. M. Peter, K. G. U. Wijayantha and A. A. Tahir, *Faraday. Discuss.,* 2012, **155**, 309-322.
6. J. Kruger, R. Plass, M. Gratzel, P. J. Cameron and L. M. Peter, J. Phys. Chem. B., 2003, **107**, 7536-7539.
7. H. Dotan, K. Sivula, M. Gratzel, A. Rothschild and S. C. Warren, *Energ. Environ. Sci.,* 2011, **4**, 958-964.
8. A. B. Murphy, P. R. F. Barnes, L. K. Randeniya, I. C. Plumb, I. E. Grey, M. D. Horne and J. A. Glasscock, *Int. J. Hydrogen. Energ.,* 2006, **31**, 1999-2017.
9. G. M. Wang, H. Y. Wang, Y. C. Ling, Y. C. Tang, X. Y. Yang, R. C. Fitzmorris, C. C. Wang, J. Z. Zhang and Y. Li, *Nano. Lett.,* 2011, **11**, 3026-3033.
10. H. Zhou and Y. R. Zhang, *J. Phys. Chem. C.,* 2014, **118**, 5626-5636.
11. Y. Li, L. Zhang, A. Torres-Pardo, J. M. Gonzalez-Calbet, Y. Ma, P. Oleynikov, O. Terasaki, S. Asahina, M. Shima, D. Cha, L. Zhao, K. Takanabe, J. Kubota and K. Domen, *Nat. Commun.,* 2013, **4**, 2566.
12. M. Tomkiewicz, *J. Electrochem. Soc.,* 1979, **126**, 1505-1510.
13. G. Liu, J. Shi, F. Zhang, Z. Chen, J. Han, C. Ding, S. Chen, Z. Wang, H. Han and C. Li, *Angew. Chem. Int. Ed.,* 2014, **53**, 7295-7299.
14. A. I. Nguyen, M. S. Ziegler, P. Ona-Burgos, M. Sturzbecher-Hohne, W. Kim, D. E. Bellone and T. D. Tilley, *J. Am. Chem. Soc.,* 2015, **137**, 12865-12872.
15. R. Chakrabarty, S. J. Bora and B. K. Das, *Inorg. Chem.,* 2007, **46**, 9450-9462.